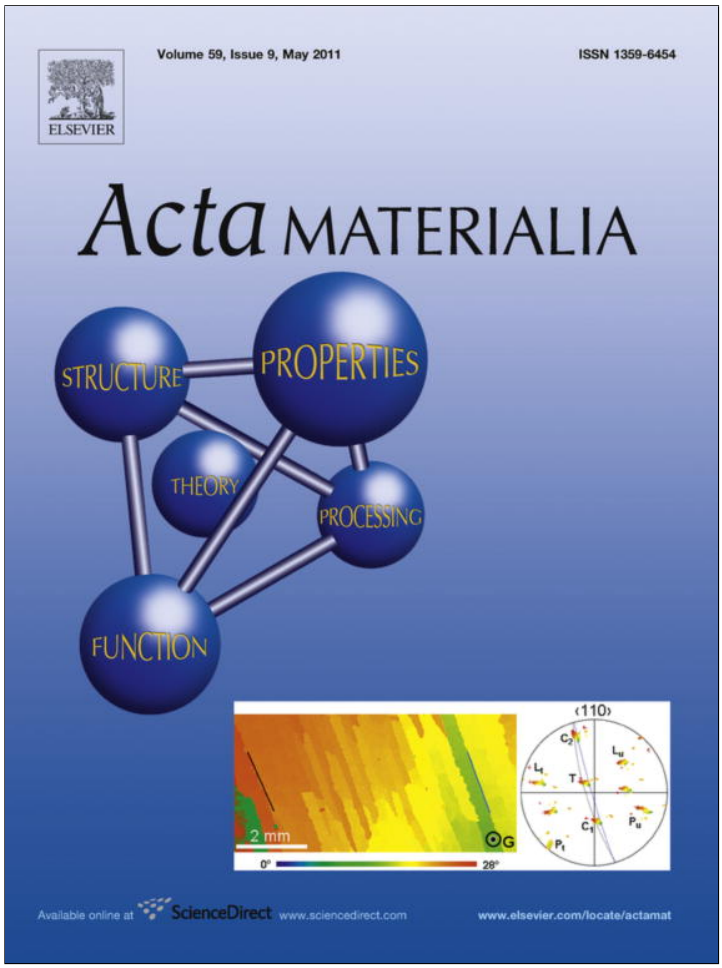

Available online at www.sciencedirect.com
ScienceDirect
Acta Materialia 59 (2011) 3364–3372
Acta MATERIALIA
www.elsevier.com/locate/actamat

Atomistic processes controlling flow stress scaling during compression of nanoscale face-centered-cubic crystals

Frederic Sansoz *

School of Engineering and Materials Science Program, The University of Vermont, Burlington, VT 05405, USA

Received 31 October 2010; received in revised form 2 February 2011; accepted 4 February 2011

Abstract

The size dependence of strength observed in submicrometer face-centered-cubic (fcc) metallic crystals under uniform deformation depends on the interaction of pre-existing dislocations with surfaces. To date, however, the dislocation processes controlling flow stress scaling in fcc crystals less than 100 nm in size have remained an open question due to limited knowledge on microstructural evolution during deformation in such small volumes. Here, molecular dynamics computer simulations employing a technique of high-temperature annealing and quenching on porous crystals were used to generate complex dislocation microstructures in sub-75 nm Cu pillars with high initial dislocation densities of 10^{16} m^{-2}, which made it possible to quantitatively examine their evolution during compression as a function of pillar diameter. These simulations reveal a transition from a state of dislocation exhaustion, where mobile dislocations are lost at the free surface and the dislocation density steadily decreases, to a regime of intermittent plastic flow between elastic loading and source-limited activation inside the pillars. It is shown that plastic flow stresses predicted during dislocation exhaustion regime exhibit little to no size dependence, while pronounced size effects are found during source-limited activation. Remarkably, the relationship between flow stress predicted at 5% strain and diameter is found to follow closely the power-law dependence reported in past experiments with larger Cu crystals and smaller densities. A deformation mechanism map, expressed in terms of diameter, is developed and used to elucidate the origin of size-dependent plasticity in nanoscale fcc crystals.

Keywords: Crystal plasticity; Dislocation density; Plastic flow properties; Size dependence; Nanomaterials

1. Introduction

Knowledge of size effects on plastic deformation is of fundamental importance to understanding plasticity and fracture in low-volume materials for applications. Uniform deformation of submicron-scale metallic pillars has become ubiquitous to studying the dependence of plasticity on sample size at the nanoscale [1–7]. In recent years, most experimental evidence has proved that the mechanical properties of nanoscale compression pillars in face-centered-cubic (fcc) metals such as Al, Au, Cu and Ni are characterized by an intermittency of plastic flow with repeated load jumps and rises at stress levels considerably higher than those attained in bulk metals [1–16]. In addition, past experimental studies [1–3,5–9,11,13–19] have shown that the plastic flow stress σ measured at 5% or 10% strain in fcc metals displays a power-law scaling of the type $\sigma \propto D^{-n}$, with D the diameter and n a scaling exponent varying between 0.4 and 1.0, where it should be understood that some uncertainty remains due to the difficulty in conducting these measurements. To observe this behavior, the common experimental method relies on carving out cylindrical microcrystals from bulk metals using focused ion beam (FIB) milling [1–3]. This fabrication technique produces dislocation densities in excess of the initial defect density present in the metal due to FIB-induced surface damage [3,12,20–22]. FIB ion bombardment is known to cause the formation of small dislocation loops that penetrate more significantly inside the pillar volume as the

* Tel.: +1 802 656 3837; fax: +1 802 656 3358.
E-mail address: frederic.sansoz@uvm.edu

1359-6454/$36.00
doi:10.1016/j.actamat.2011.02.011

diameter decreases [6,12,20]. As dislocations are the primary carriers of plasticity in metals, studying the influence of initial dislocation densities on size-dependent plasticity at the nanoscale has become a focal point for research. Alternatively, Greer and co-workers [16,23] have devised a bottom-up approach using direct electrodeposition to create ⟨1 1 1⟩ Cu pillars with diameters in the 100–500 nm range without FIB-like surface damage. Their approach produced Cu pillars with initial dislocation density as high as 1.5×10^{14} m^{-2}, which in reality corresponds to the presence of very few dislocations in these small volumes [16]. Surprisingly, the exponent n in the scaling relationship between flow stress and diameter remains almost identical in Cu nanopillars regardless of the fabrication method [16]. These results therefore confirm that the evolution of pre-existing mobile dislocations and their interaction with free surfaces during deformation play a key role in the size-dependent plasticity of metallic compression nanopillars.

Discrete dislocation dynamics (DDD) computer simulations have been extensively used in order to study the mechanisms controlling flow stress scaling in microcrystals with random networks of dislocations [21,24–39]. These studies have predicted two types of size-dependent hardening mechanism relevant to the compression of submicrometer fcc pillars. One mechanism, source-truncation hardening, depicts the breaking of Frank–Read loops pinned at artificial points or by cross-slip processes [36], and intersecting the free surface to form two single-arm sources of shorter length, which are kept inactive until there is a sufficient rise in the applied stress [27,28,34,36]. A second mechanism, hardening by dislocation starvation, was proposed when the rate of dislocation escape at free surfaces is found to exceed that for dislocation multiplication, to the extent that plastic deformation becomes source-limited [24,25,30,32,33,35]. However, thermally activated processes at atomic scale, such as surface-assisted dislocation nucleation [40,41], remain largely unexplored in nanopillar plasticity, because the DDD simulation technique cannot easily capture such processes. Also, prior attempts made to use atomistic simulations to reproduce the size-dependent hardening behavior observed experimentally in fcc compression nanopillars have not been successful because defect-free crystals have always been considered in this type of simulation [42,43].

Here, we use a new atomistic simulation technique to describe the processes of microstructure evolution and plastic flow scaling at atomic scale in small Cu nanopillars containing high initial dislocation densities. Remarkably, these simulations predict the same flow stress scaling as that observed experimentally in nanoscale fcc crystals with larger diameters and smaller densities. A deformation mechanism map is developed based on a large number of molecular simulations on crystals with different diameters and initial microstructures. This map is used to show that the size-dependent emission of new dislocations from small immobile defects inside the pillars governs flow stress scaling in nanoscale Cu crystals generated by the present technique, whereas neither source-truncation nor dislocation-exhaustion processes are found to contribute significantly to this effect.

2. Methods

Molecular dynamics (MD) simulations were conducted with the software LAMMPS [44] using an embedded-atom-method potential for pure Cu [45]. This study focuses on single-crystalline ⟨1 1 1⟩ Cu pillars with different diameters between 10.8 nm and 72.3 nm, using models with up to 10.5 million atoms. The initial pillar structures consisted of [1 1 1]-oriented cylindrical crystals with a circular cross-section. All directions were kept free except for the loading direction. Periodic boundary conditions were imposed along the [1 1 1] loading axis with a periodic length equal to 30 nm, which was important to ensure no effects of boundary and aspect ratio on the predicted plastic flow stresses. The periodic length was doubled in one of the simulations to verify that the simulated flow stresses were not significantly influenced by this dimension. Complex networks of dislocations were generated in each pillar in two steps. First, a fraction of 10% of atoms was randomly removed from the system. Second, a heat treatment consisting of both high-temperature annealing and quenching was simulated on each porous crystal under zero applied loading in the isothermal–isobaric ensemble (constant number of particles, pressure and temperature, NPT) using a Nosé–Hoover thermostat: heating in 50 ps from 300 K to 1278 K (i.e., 100 K below the melting temperature for Cu), annealing at 1278 K for up to 200 ps, quenching to 300 K in 50 ps (Fig. A1). Different microstructures were generated for the same pillar diameter by varying the random seed in the atom removal step, or by increasing the annealing time at 1278 K. In order to obtain an equilibrium state before loading, an additional annealing under zero load was performed for 50 ps at the temperature of deformation (300 K). The nanopillars were deformed in compression by shrinking the simulation box along the loading direction at an engineering strain rate of 5×10^7 s^{-1} [46]. A Nosé–Hoover thermostat was used to maintain a constant temperature of 300 K during deformation in canonical ensemble (constant number of particles, volume and temperature, NVT). The time step was 5 fs. The local crystal structures were recorded at 10 ps interval (2000 steps) using the analysis by Ackland and Jones [47]. Snapshots of simulation were generated with the software AtomEye [48]. The calculation of stress in the loading direction is described elsewhere [46].

3. Results

3.1. Dynamic evolution of microstructure

A cylindrical Cu nanopillar with a circular cross-section of 43.4 nm in diameter produced by the above technique is

shown in Fig. 1a. The simulated microstructures consisted of an array of curved $\langle 1\,1\,0\rangle$ dislocations on different $\{1\,1\,1\}$ slip planes typical of fcc metals, noting that the maximum Schmid factor was 0.272 for this pillar orientation. All dislocations were dissociated into $\{1\,1\,1\}\langle 1\,1\,\bar{2}\rangle$ partial dislocations connected by stacking faults, as indicated by the hexagonal-close packed (hcp) atoms in yellow in Fig. 1a. The microstructures also contained some small stacking-fault tetrahedra and point defects such as vacancies appearing in red in this figure. The initial fraction of hcp atoms obtained at equilibrium state in the present models was between 0.75% and 3.25% of the total number of atoms. The corresponding dislocation density ρ was estimated via the formula

$$\rho = \frac{V_{hcp}}{\langle \eta \rangle}\rho_{at} \tag{1}$$

with V_{hcp} the fraction of hcp atoms, $\langle \eta \rangle$ the average number of hcp atoms in a stacking-fault ribbon connecting two Shockley partials (per unit length of dislocation), and ρ_{at} the atomic density (76.2 nm^{-3}). To establish this equation, an assumption was made that the dislocations were all dissociated with a stacking fault of constant width of $\langle \eta \rangle$ hcp atoms. As such, the total length of dislocation was equal to the total number of hcp atoms present in the system divided by $\langle \eta \rangle$. In addition, it was considered that the pillar volume was equal to the ratio of total number of atoms to ρ_{at}. In the current simulations, it was estimated that $\langle \eta \rangle \sim 108.4\ \text{nm}^{-1}$, which corresponds to a range of dislocation densities between $5.9 \times 10^{15}\ \text{m}^{-2}$ and $2.3 \times 10^{16}\ \text{m}^{-2}$. Such initial densities are one order of magnitude larger than those measured experimentally in FIB-machined metallic nanopillars of 160 nm in diameter, $10^{15}\ \text{m}^{-2}$ [12]. Nevertheless, it is expected for smaller nanopillars to present higher dislocation densities [15,16,22]; for example, ρ scales with $1/D$ if we assume that the height of the pillar h is constant and that only one straight dislocation of total length D glides inside a circular pillar of volume $h\pi(D/2)^2$. Therefore, the smallest dislocation density attainable in pillars with a diameter and a periodic length equal to 43.4 nm and 30 nm, respectively, similar to that shown in Fig. 1a, is equal to $9.7 \times 10^{14}\ \text{m}^{-2}$.

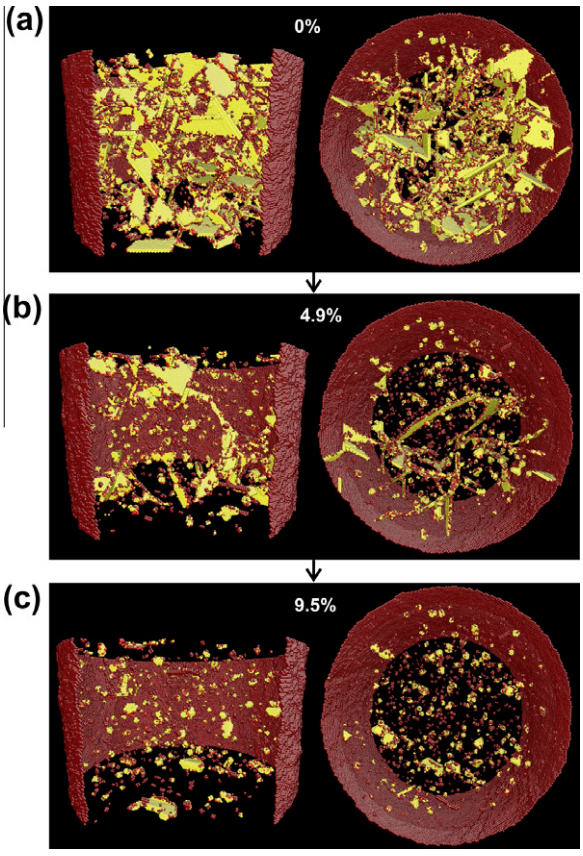

Fig. 1. Molecular dynamics simulation of a $\langle 1\,1\,1\rangle$ Cu nanopillar with a diameter of 43.4 nm and an initial dislocation density of $1.7 \times 10^{16}\ \text{m}^{-2}$ under compressive loading. Atomic-level snapshots of microstructure viewed from the top and front sides of the pillar at true compression strains of (a) 0%, (b) 4.9% and (c) 9.5%. Atoms in hcp arrangement are colored in yellow. Non-coordinated atoms, such as atoms near vacancies and free surfaces, are shown in red. Atoms in fcc arrangement are not shown for clarity.

Fig. 1b and c presents different snapshots of simulation of the microstructure evolution in this 43.4 nm diameter Cu nanopillar under compressive loading. These figures reveal a pronounced effect of dislocation starvation resulting in the paucity of mobile dislocations, as clearly shown in the model for a compression strain of 9.5%. This key result agrees with past experimental observations in fcc metal nanopillars below 500 nm in diameter [5,12,15,16], whereas it was predicted in previous DDD simulation studies that the total dislocation density is either constant or even increases in the course of deformation [28,32,34,35,37]. Furthermore, we find that two regimes of plastic deformation have been successively reached in this pillar as the applied strain increases. Using the evolution of the fraction of hcp atoms as a function of applied strain, Fig. 2a shows that the first regime is a progressive stage of dislocation exhaustion, up to a critical strain of 5.4%, during which the density of mobile dislocations decreases from $1.7 \times 10^{16}\ \text{m}^{-2}$ to $3.6 \times 10^{15}\ \text{m}^{-2}$ at a quasi-constant escape rate. This effect was caused by significant dislocation annihilation at free surfaces, whose dynamic processes are detailed in Movie S1 for compression strains up to 9.5%. A more refined sequence, Movie S2, starting at a true strain of 4.5%, clearly shows the occurrence of source-truncation effects and spiral sources, similar to the mechanisms observed in submicron-scale single crystals during DDD simulations [28,29,36,37] or in situ experiments [49]. The pinning points of such spiral dislocations were due to cross-slip events as shown in Fig. 3. In contrast to past studies, however, the pinning points were found to be highly mobile and easily absorbed by the free surface upon compression, which caused no multiplication of dislocations in these pillars. Therefore, the rate of dislocation escape was significantly larger than that for dislocation nucleation, thereby explaining the decrease in dislocation density. In the second regime of plastic deformation,

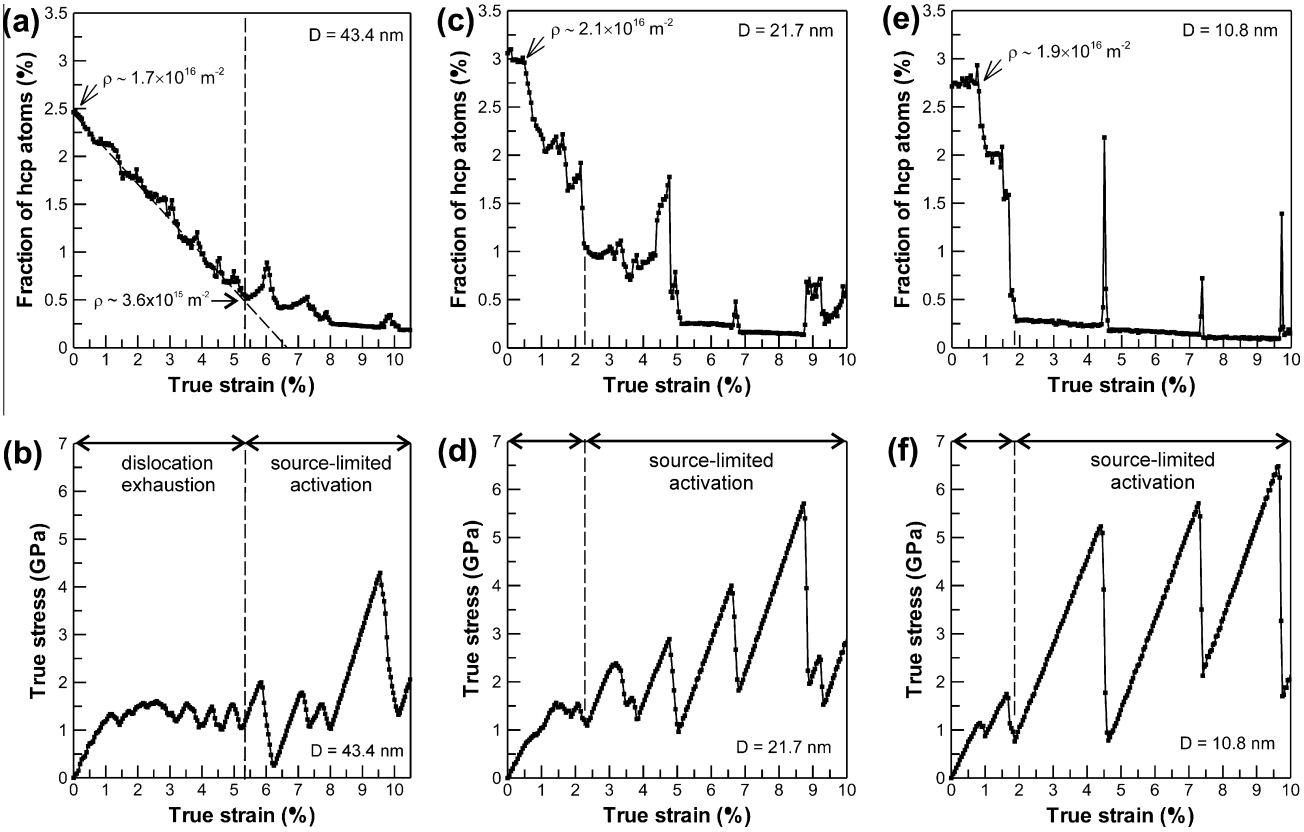

Fig. 2. Compression behavior of simulated Cu nanopillars with diameters equal to 43.4, 21.7 and 10.8 nm and an initial dislocation density of $\sim 2 \times 10^{16}$ m^{-2}. (a, c, and e) Evolution of the fraction of hcp atoms as a function of applied strain. (b, d, and f) true stress–strain curves simulated at 300 K under constant strain rate.

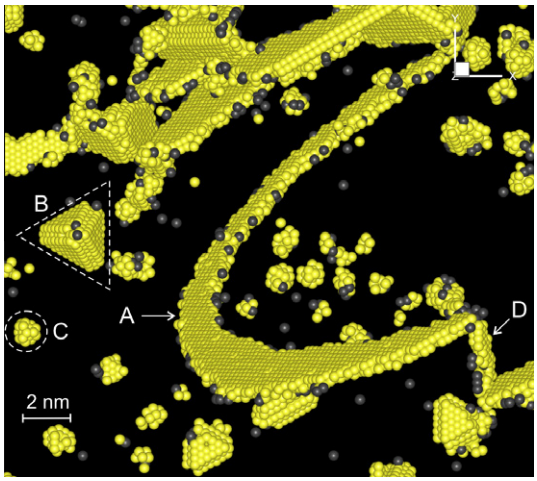

Fig. 3. Close-up view on microstructure inside a 43.4 nm diameter pillar at true compression strain of 5%. (a) Extended spiral dislocation; (b) stacking-fault tetrahedron; (c) immobile defect cluster; (d) pinning point due to cross-slip process. The crystal directions shown correspond to $X = [1\,1\,\bar{2}]$, $Y = [\bar{1}\,1\,0]$ and $Z = [1\,1\,1]$.

Fig. 2a and Movie S1 show that the behavior for strains larger than 5.4% is related to a series of elastic loading interrupted by dislocation avalanches. This phenomenon was manifested by the successive emission of new dislocation loops on a limited number of immobile defects inside the pillar, such as small stacking-fault tetrahedra, which were much smaller than the extended mobile dislocations (Fig. 3). Emission events were found to start systematically on the largest defect to continue with the smallest ones. During this regime, referred to as source-limited activation in the following, the dislocation density no longer decreases in a significant manner (Fig. 2a), because both emission and exhaustion of dislocations operate at the same rate.

Furthermore, Fig. 2c and e, and the snapshots of simulation presented in Figs. 4 and 5, confirm the existence of a transition from dislocation exhaustion to source-limited activation in smaller nanopillars with a diameter equal to 21.7 nm and 10.8 nm. The disappearance of all pre-existing dislocations is also made clear in the dynamic evolution of microstructures presented at second 18 and second 7 in Movies S3 and S4, respectively. A salient feature is that the regime of source-limited activation did occur earlier in these nanopillars than in the pillar with a diameter of 43.4 nm (Fig. 2a). We can interpret this observation by the decrease in the number of pre-existing dislocations via size reduction, when comparing Fig. 1a to Figs. 4a and 5a, as discussed below.

3.2. Flow stress scaling

We find in Fig. 2b, d and f that significant serrated-like behavior is caused in the stress–strain curves simulated at

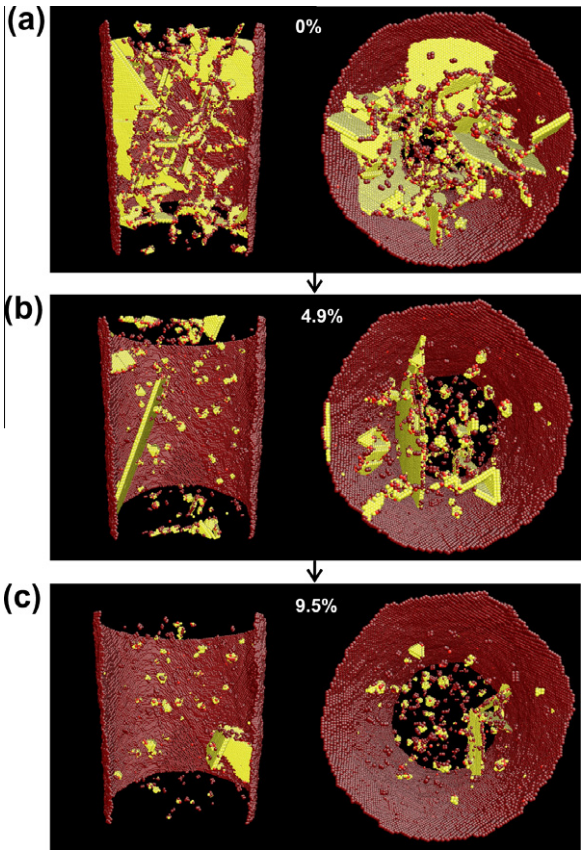

Fig. 4. Molecular dynamics simulation of a ⟨1 1 1⟩ Cu nanopillar with a diameter of 21.7 nm and an initial dislocation density of $2.1 \times 10^{16}\,m^{-2}$ under compressive loading. Atomic-level snapshots of microstructure viewed from the top and front sides of the pillar at true compression strains of: (a) 0%, (b) 4.9% and (c) 9.5%.

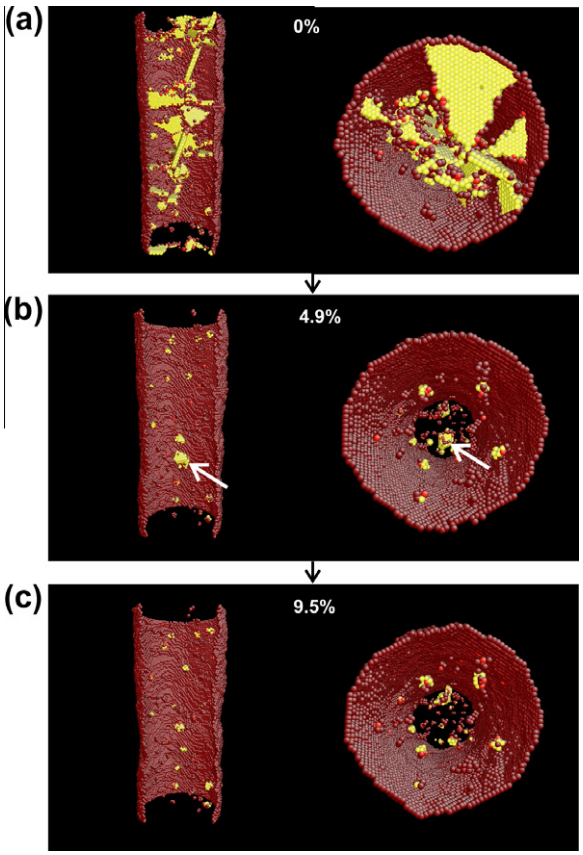

Fig. 5. Molecular dynamics simulation of a ⟨1 1 1⟩ Cu nanopillar with a diameter of 10.8 nm and an initial dislocation density of $1.9 \times 10^{16}\,m^{-2}$ under compressive loading. Atomic-level snapshots of microstructure viewed from the top and front sides of the pillar at true compression strains of: (a) 0%, (b) 4.9% and (c) 9.5%. The arrow in (b) shows a small dislocation loop on the pillar axis serving as a source for a new dislocation.

300 K due to the repetition of dislocation glide and escape events at the surface, like the intermittent plastic flow reported experimentally in nanoscale Cu pillars [16]. However, it is also evident that the mechanical behavior is markedly different, depending on whether the plastic deformation proceeds by dislocation exhaustion or source-limited activation. In particular, Fig. 2b shows that a constant flow stress of 1.34 ± 0.16 GPa is attained below 5.4% strain, and that the overall plastic flow presents no strain-hardening effect during dislocation exhaustion. By contrast, in the same figure, a significant increase in stress is found at the onset of source-limited activation corresponding to the elastic loading of the pillar followed by a stress jump at 4.3 GPa. A similar response could be observed in the yielding of defect-free fcc whiskers, where the mechanism of surface dislocation nucleation is found to be predominant [46,50,51]. However, a major difference with this case is that, here, the sites for dislocation emission were all found inside the nanopillars instead of the free surface.

A comparison of the three stress–strain curves presented in Fig. 2 for different pillar diameters allows us to conclude that flow stresses during dislocation exhaustion regime do not significantly vary with a change in diameter, as opposed to those during source-limited activation. It also appears that achieving source-limited activation and higher flow stresses requires less applied strain when the sample size decreases, as discussed below.

Furthermore, we compared these atomistic results to experimental data by Jennings et al. [16], which were obtained under constant loading rate, by measuring the maximum flow stress attained along each stress–strain curve up to a fixed amount of strain (5%). The maximum flow stresses for compression strains up to 5% for 24 atomistic simulations with different initial microstructures are represented in Fig. 6, as a function of pillar diameter, along with the experimental data of flow stresses at 10% strain in ⟨1 1 1⟩ Cu nanopillars. Remarkably, this figure shows that the maximum flow stresses predicted by the present simulation technique closely follow the scaling exponent of 0.61 fitted on experimental data obtained with larger crystal diameters and smaller dislocation densities ($\sim 10^{14}\,m^{-2}$). This finding therefore proves that the same effect of plastic flow scaling under compression exists in ⟨1 1 1⟩ Cu nanopillars with diameters smaller than 100 nm.

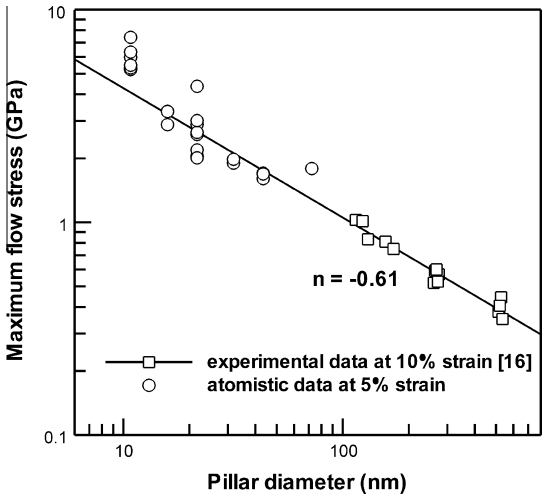

Fig. 6. Log–log plot of maximum flow stress up to 5% strain as a function of pillar diameter from 24 atomistic simulations with different initial microstructures. Experimental data of flow stresses obtained in ⟨1 1 1⟩ Cu nanopillars at 10% strain are reported for comparison.

4. Discussion

A deformation mechanism map for nanoscale ⟨1 1 1⟩ Cu crystals, expressed in terms of diameter and based on the above simulations, is presented in Fig. 7. Two regimes of plastic deformation can be distinguished in this figure for a given diameter, i.e., mobile dislocation exhaustion at low applied strains and source-limited activation at large applied strains. Outside the data scattering inherent to the stochastic nature of these atomistic processes [11], this figure clearly displays a power-law trend with an exponent close to unity for the limit between the two regimes as a function of pillar diameter. A geometrical analysis of the number of mobile dislocations N present in the system

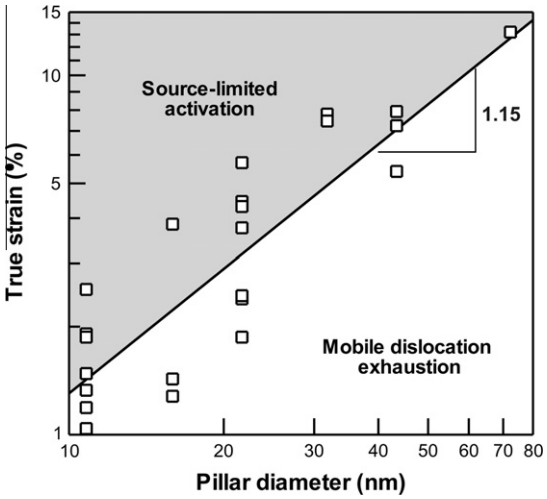

Fig. 7. Deformation mechanism map for nanoscale ⟨1 1 1⟩ Cu crystals with initial dislocation densities of $\sim 10^{16}\,\mathrm{m}^{-2}$ as a function of pillar diameter.

before compression, and their average length $\langle L \rangle$, can be used to interpret this trend. Past DDD studies have suggested taking the pillar radius as an upper bound for the length of dislocation sources in nanoscale crystals [26,27,34]. In particular, assuming $\langle L \rangle \sim D/2$ prior to deformation agrees well with the present simulations. As the initial dislocation density ρ_i is almost constant between each pillar, this assumption leads to a monotonic dependence of N on diameter, such as

$$N \approx \rho_i h \pi (D/2) \tag{2}$$

Also we note in Fig. 2a that ρ decreases almost linearly with the applied strain during dislocation exhaustion. Thus the rate of dislocation loss at surfaces can be regarded as nearly constant, which gives

$$\varepsilon_c \propto N \tag{3}$$

where ε_c is the strain at the onset of source-limited activation. Therefore, combining Eqs. (2) and (3) justifies why the regime transition, i.e. ε_c, varies linearly with the pillar diameter in Fig. 7.

The implications of this deformation map are threefold. First, a key finding in the present study is that neither source-truncation nor dislocation-starvation processes causes significant size effect on flow stresses during the regime of dislocation exhaustion. More specifically, Fig. 2b has revealed that dislocation glide is governed by a unique flow stress, which could result from the narrow length distribution of dislocations generated in these small nanopillars, and that the overall plastic flow presents no strain-hardening during dislocation exhaustion. Previous experimental and computational studies [13,19,33] have shown that the size dependence of flow stress in single-crystalline fcc micropillars is related to significant strain-hardening effects after slip activation. This supports our finding that no size effect took place during dislocation exhaustion as shown in the three stress–strain curves in Fig. 2. To further confirm this hypothesis, Fig. 8 shows a log–log representation of the maximum flow stresses predicted at true compression strains up to 2% and 10%. This figure shows that the maximum flow stresses for strains up to 2% diverge noticeably from the experimental trend in Fig. 6, and show little to no size dependence, while dislocation exhaustion is predominant at this stage of deformation in most nanopillars as shown in Fig. 7. On the contrary, plastic flow stresses predicted at strains up to 10% exhibit strong size effects with a power-law scaling behavior close to that obtained in Fig. 6. It should be pointed out that source-limited activation takes place in all models deformed at 10% strain, except for the nanopillar of 72.3 nm in diameter. In this case, the regime transition occurred at ~14% strain, so no significant variation in maximum flow stress was found for strains between 2% and 10%, as shown in Figs. 6 and 8.

Second, a conflicting observation has been made in the past between experiments and DDD simulations, because

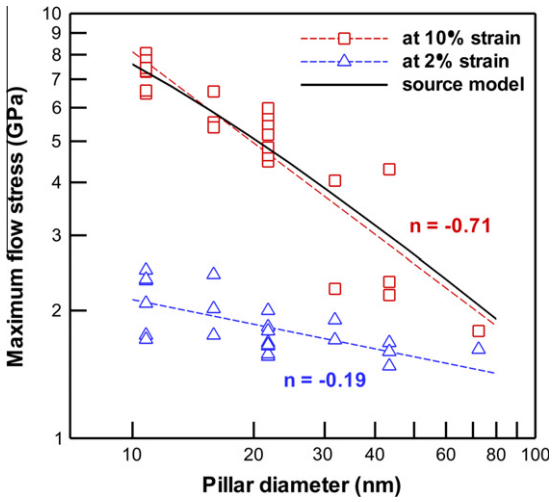

Fig. 8. Log–log plot of maximum flow stress for strains up to 2% and 10%, as a function of pillar diameter. Power-law scaling trends are indicated by dashed lines. The solid line represents the source activation model described by Eq. (4).

intermittent plastic flow and flow stress scaling in FIB-machined fcc nanopillars were observed at much larger compression strains in experiments [5,12,15,16] than in DDD simulations [24,28,33,34,37–39]. This discrepancy can be resolved by using Fig. 7. Owing to Eq. (2), the transition line in the deformation mechanism map is expected to keep the same slope, as a function of diameter, while shifting downward for smaller dislocation densities. Therefore, the above difference may result from the absence of significant dislocation loss predicted in DDD simulations, as opposed to direct experimental observations [12]. However, aside from employing different methods to obtain an accurate measure of flow stress, it is possible to postulate from the present atomistic study that the size dependence of strength in nanoscale fcc crystals under compression is controlled by the same underlying mechanism in both experiments and DDD simulations, i.e. source-limited activation.

Third, the transition to source-limited activation can provide a predictive understanding of flow stress scaling in the crystals generated by the present technique. It was argued that source-limited deformation could result in the nucleation of new dislocation at surfaces [7,41], but direct evidence for such mechanism have been difficult to confirm; for example, in situ TEM experiments have been able to capture the operation of single-ended sources inside submicron-scale Al single crystals [49]. It was found here that source-limited activation is controlled by the emission of dislocation loops from small immobile defects inside the pillars, such as small stacking-fault tetrahedra and defect clusters as shown in Fig. 3. By way of illustration, the arrow in Fig. 5b shows a small defect inside a 10.8 nm diameter pillar, which serves as a source for a new double-ended dislocation that escapes the crystal easily (see Movie S5). This particular source is located at the center of the pillar, where image stresses due the free surface are small and can be neglected [30]. The uniaxial stress to activate this source is therefore [26,52]

$$\sigma_{source} = \frac{1}{m} \cdot \frac{\alpha' G b}{L} \ln\left(\frac{L}{b}\right) \tag{4}$$

where m is the Schmid factor for the active slip system, L is the actual size of the double-ended source, G is the shear modulus, b is the magnitude of Burgers vector, and the parameter α' is the source-length coefficient that varies with the exact nature of the source (for double-ended Franck–Read sources, Ref. [26] suggests taking $\alpha' = 0.187$). This source activation model is represented in Fig. 8 using $m = 0.272$, $G = 42$ GPa, $b = 0.255$ nm, and $L = D/5$. The latter reflects the fact that the average size of defects remaining in the system at a fixed amount of strain depends on the diameter, which is also related to the deformation mechanism map in Fig. 7, and is much smaller than the average dislocation length prior to deformation ($\langle L \rangle \sim D/2$). Despite this approximation, Fig. 8 shows that the source model is in excellent agreement with the plastic flow scaling predicted by atomistic simulation at 10% compression strain, which therefore confirms that source-limited activation is responsible for the scaling behavior observed in the strength of nanoscale fcc crystals. Also, a caveat of the current simulation technique is that strain rates imposed during nanopillar deformation are unrealistically high compared to experiments. However, it can be hypothesized that smaller strain rates would not change the present conclusions because it has been observed experimentally that nanoscale fcc crystals deformed in tension would be more rapidly starved out of mobile dislocations as the strain rate decreases [49]. This therefore suggests conducting a more detailed study of thermal activation at different temperatures and strain rates during source-limited deformation and related size effects in Cu nanopillars.

5. Conclusion

A simulation technique has been developed to provide atomic-scale insights into the microstructural evolution of nanoscale pillars in fcc metals under uniform deformation, which is an important step forward to understanding size effects in crystal plasticity relevant for nanoscale applications. This technique has enabled the simulation of key mechanisms of nanoscale plasticity observed in the past with different methods, such as in situ nanocompression experiments or DDD simulations. This study has shown that neither source-truncation nor dislocation-exhaustion processes significantly contributes to the size dependence of strength in nanoscale ⟨1 1 1⟩ Cu crystals generated by the above technique, whereas flow stress scaling can be associated with the emission of new dislocations from small immobile defects inside the pillars. Also, the present technique is general, which may open up new opportunities

to investigate complex phenomena in more extreme environments, such as those involving thermal exposure or radiation damage.

Acknowledgments

Support from NSF CAREER program (Grant DMR-0747658) and the computational resources provided by the Vermont Advanced Computing Center (NASA Grant NNX06AC88G) are gratefully acknowledged.

Appendix A

See Fig. A1.

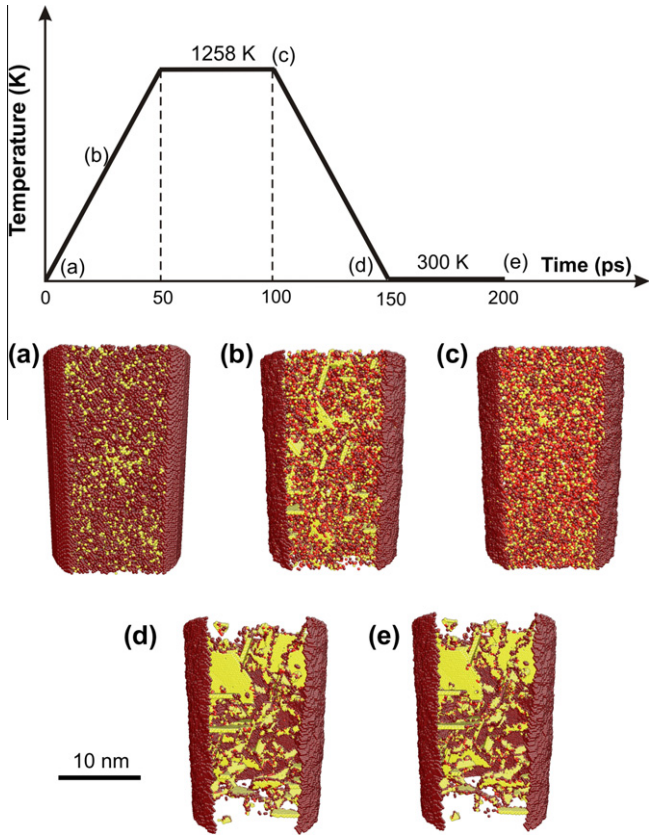

Fig. A1. Making of a random dislocation network in a ⟨1 1 1⟩ cylindrical Cu crystal with an initial porosity of 10% by technique of high-temperature annealing and quenching using molecular dynamics simulation. Atoms in hcp arrangement are colored in yellow. Non-coordinated atoms such as atoms near free surfaces and vacancies are shown in red. Atoms in fcc arrangement are not shown for clarity. (For interpretation of the references to color in this figure legend, the reader is referred to the web version of this article.)

Appendix B. Supplementary material

Supplementary data associated with this article can be found, in the online version, at doi:10.1016/j.actamat.2011.02.011.

References

[1] Uchic MD, Dimiduk DM, Florando JN, Nix WD. Science 2004;305:986.
[2] Dimiduk DM, Uchic MD, Parthasarathy TA. Acta Mater 2005;53:4065.
[3] Greer JR, Oliver WC, Nix WD. Acta Mater 2005;53:1821.
[4] Dimiduk DM, Woodward C, LeSar R, Uchic MD. Science 2006;312:1188.
[5] Greer JR, Nix WD. Phys Rev B 2006;73:245410.
[6] Kiener D, Motz C, Schoberl T, Jenko M, Dehm G. Adv Eng Mater 2006;8:1119.
[7] Volkert CA, Lilleodden ET. Philos Mag 2006;86:5567.
[8] Brinckmann S, Kim JY, Greer JR. Phys Rev Lett 2008;100:155502.
[9] Frick CP, Clark BG, Orso S, Schneider AS, Arzt E. Mater Sci Eng A – Struct Mater Prop Microstruct Process 2008;489:319.
[10] Maass R, Van Petegem S, Grolimund D, Van Swygenhoven H, Kiener D, Dehm G. Appl Phys Lett 2008;92:071905.
[11] Ng KS, Ngan AHW. Acta Mater 2008;56:1712.
[12] Shan ZW, Mishra RK, Asif SAS, Warren OL, Minor AM. Nat Mater 2008;7:115.
[13] Maass R, Van Petegem S, Ma DC, Zimmermann J, Grolimund D, Roters F, et al. Acta Mater 2009;57:5996.
[14] Kim JY, Greer JR. Acta Mater 2009;57:5245.
[15] Lee SW, Han SM, Nix WD. Acta Mater 2009;57:4404.
[16] Jennings AT, Burek MJ, Greer JR. Phys Rev Lett 2010;104:135503.
[17] Uchic MD, Shade PA, Dimiduk DM. Ann Rev Mater Res 2009;39:361.
[18] Kiener D, Grosinger W, Dehm G. Scr Mater 2009;60:148.
[19] Kiener D, Minor AM. Acta Mater 2011;59:1328.
[20] Kiener D, Motz C, Rester M, Jenko M, Dehm G. Mater Sci Eng A – Struct Mater Prop Microstruct Process 2007;459:262.
[21] El-Awady JA, Woodward C, Dimiduk DM, Ghoniem NM. Phys Rev B 2009;80:104104.
[22] Norfleet DM, Dimiduk DM, Polasik SJ, Uchic MD, Mills MJ. Acta Mater 2008;56:2988.
[23] Burek MJ, Greer JR. Nano Lett 2010;10:69.
[24] Benzerga AA, Shaver NF. Scr Mater 2006;54:1937.
[25] Tang H, Schwarz KW, Espinosa HD. Acta Mater 2007;55:1607.
[26] Rao SI, Dimiduk DM, Tang M, Parthasarathy TA, Uchic MD, Woodward C. Philos Mag 2007;87:4777.
[27] Parthasarathy TA, Rao SI, Dimiduk DM, Uchic MD, Trinkle DR. Scr Mater 2007;56:313.
[28] Rao SI, Dimiduk DM, Parthasarathy TA, Uchic MD, Tang M, Woodward C. Acta Mater 2008;56:3245.
[29] Tang H, Schwarz KW, Espinosa HD. Phys Rev Lett 2008;100:185503.
[30] Weinberger CR, Cai W. Proc Natl Acad Sci USA 2008;105:14304.
[31] Greer JR, Weinberger CR, Cai W. Mater Sci Eng A – Struct Mater Prop Microstruct Process 2008;493:21.
[32] Benzerga AA. Int J Plast 2008;24:1128.
[33] Guruprasad PJ, Benzerga AA. J Mech Phys Solids 2008;56:132.
[34] El-Awady JA, Wen M, Ghoniem NM. J Mech Phys Solids 2009;57:32.
[35] Benzerga AA. J Mech Phys Solids 2009;57:1459.
[36] Lee SW, Nix WD. Mater Sci Eng A – Struct Mater Prop Microstruct Process 2010;527:1903.
[37] Zhou CZ, Biner SB, LeSar R. Acta Mater 2010;58:1565.
[38] Motz C, Weygand D, Senger J, Gumbsch P. Acta Mater 2009;57:1744.
[39] Weygand D, Poignant M, Gumbsch P, Kraft O. Mater Sci Eng A – Struct Mater Prop Microstruct Process 2008;483:188.
[40] Zhu T, Li J, Samanta A, Leach A, Gall K. Phys Rev Lett 2008;100:025502.
[41] Nix WD, Lee SW. Philos Mag 2011. doi:10.1080/14786435.2010.50214.
[42] Marian J, Knap J. Int J Multiscale Comput Eng 2007;5:287.

[43] Cao A, Wei YG, Mao SX. Scr Mater 2008;59:219.
[44] Plimpton SJ. J Comp Phys 1995;117:1.
[45] Mishin Y, Mehl MJ, Papaconstantopoulos DA, Voter AF, Kress JD. Phys Rev B 2001;63:224106.
[46] Deng C, Sansoz F. Nano Lett 2009;9:1517.
[47] Ackland GJ, Jones AP. Phys Rev B 2006;73:054104.
[48] Li J. Modelling Simul Mater Sci Eng 2003;11:173.
[49] Oh SH, Legros M, Kiener D, Dehm G. Nat Mater 2009;8:95.
[50] Deng C, Sansoz F. Acta Mater 2009;57:6090.
[51] Richter G, Hillerich K, Gianola DS, Monig R, Kraft O, Volkert CA. Nano Lett 2009;9:3048.
[52] Kraft O, Gruber PA, Monig R, Weygand D. Ann Rev Mater Res 2010;40:293.